Nuclear Science and Techniques (2026) 37:73
https://doi.org/10.1007/s41365-026-01884-8

α ionizing particle radiation detection and damage compensation methods for CMOS active pixel sensors

Shou-Long Xu[1] · Cui-Yue Wei[1] · Zhi-Wei Qin[1] · Shu-Liang Zou[1] · Yong-Chao Han[2] · Qing-Yang Wei[3] · You-Jun Huang[4]

Received: 26 June 2024 / Revised: 3 September 2024 / Accepted: 28 September 2024 / Published online: 3 February 2026

Abstract
In this study, the mechanism and characteristics of the response α particles and the damage caused by them in CMOS active pixel (APS) sensors were investigated. A detection and compensation algorithm for dead pixels caused by α particle ionizing radiation was proposed, and the effects of dead-pixel compensation algorithms were compared and analyzed under different parameter conditions. The experimental results show that α particle response signal has highest accuracy at 9 dB gain, with an obvious "target-ring" distribution. With increasing cumulative dose, the CMOS APS pedestal tends to saturation while dead pixels continue increasing. Though some pixel damage recovers through natural annealing, the dead-to-noise ratio increases with irradiation time, reaching 32.54% after 72 h. A hierarchical clustering dead-pixel detection method is proposed, categorizing pixels into two types: those within and outside the response event. A classification compensation strategy combining mean and majority filtering is proposed. This compensation algorithm can address dead-pixel interference without affecting α particle radiation response data. When iterated multiple times and with integration time exceeding 6.31 ms, the number of dead pixels can be effectively reduced.

Keywords CMOS active pixel sensor · α particles · Response event · Radiation damage · Dead-pixel compensation

1 Introduction

As an important branch of nuclear radiation detection [1], α-particle detection technology has important applications in surface nuclear radiation contamination detection [2, 3], radon measurement [4, 5], and neutron measurement based on the nuclear reaction method [6, 7]. Currently, the instruments used for α-particle detection mainly include gas ionization detectors [8, 9], scintillator detectors [10, 11], solid track detectors [12, 13], time-projection chambers [14, 15], and drift chambers [16]. Traditional detection methods often have problems, such as large equipment size, complex operation, and limited measurement accuracy [17]. They are also insufficient in digitalization and intelligence, and cannot meet the needs of modern scientific research and industrial production. Therefore, the development of digital and intelligent chip-level detection methods, technologies, and equipment has become an important direction for the development of α-particle detection technology.

The CMOS active pixel sensor (CMOS APS), which is a device that integrates signal detection, processing, and readout functions, has shown significant advantages in the field of nuclear radiation detection [18]. Its unique pixel-level signal-processing capabilities enable the CMOS APS to achieve high-resolution, low-noise, and high-frame-rate radiation imaging [19, 20], thereby providing a new technical approach for nuclear radiation detection. This new detection technology can not only achieve high-precision and high-sensitivity detection of α particles but also has the advantages of small size, low power consumption, and easy

This work was supported by the National Natural Science Foundation of China (No.11905102) and Hunan Provincial Postgraduate Research and Innovation Project (No. QL20230234).

✉ Shou-Long Xu
xusl@usc.edu.cn

[1] University of South China, Hengyang 421001, China

[2] China Institute of Atomic Energy, Beijing 102413, China

[3] University of Science and Technology Beijing, Beijing 100083, China

[4] Nuclear Power Institute of China, Chengdu 610213, China

integration [21, 22]. It can also realize real-time transmission and data processing, which provides core radiation monitoring, and early warning provides timely and accurate information. Currently, CMOS APS are widely used in the detection of charged particles, such as γ rays [23–25], X-rays [26–28], protons [29] and low-energy electrons [30]. The principle is that radiation interacts with the epitaxial layer material to generate electron–hole pairs, which are then collected by the space-charge region, resulting in a radiation response signal [31]. The application of CMOS APS for ionizing particle detection is known as nuclear radiation detection. Scholars have launched new explorations into detection methods, with limited research on alpha particle detection. Research on α particle radiation effect of CMOS APS will advance digital and chip-based development in α particle detection [32]. This detection technology faces challenges in optimizing methods and radiation damage [33, 34]. Radiation damage in CMOS devices includes ionizing type, caused by radiation-induced electron displacement, and non-ionizing type, resulting from atom displacement [35]. The radiation damage by α particles to active pixel sensors primarily reflects the displacement effect. With advancing reactor and accelerator technology, research has focused on displacement effects in neutrons and protons [36], while studies on alpha particle radiation damage remain limited. For noise detection and compensation, current methods include statistical models, machine learning, transform domain techniques, and image processing [37]. Statistical models detect abnormalities through pixel distribution and reconstruct images, offering good noise robustness but with high computational complexity [38]. Deep learning methods using computational neural networks (CNNs) and generative adversarial networks (GANs) have progressed in image detection and restoration [39, 40], enabling automatic dead-pixel detection, but require substantial data and computing resources. Transform domain methods analyze noise through spectral analysis [41], while image processing methods use edge detection and segmentation for noise identification [42]. Though computationally simple, these methods have limited effectiveness for complex scenes. Current algorithms, while partially effective for noise identification and compensation, struggle with refined detection and compensation for radiation damage noise.

In this study, we conducted α-particle ionizing radiation experiments on CMOS APS to elucidate the "target-ring" distribution characteristics of α-particle radiation response events. Based on a comprehensive analysis of the dark signal characteristics of pedestals, noise, and dead pixels before and after APS radiation damage, a hierarchical clustering dead-pixel detection method was proposed to achieve refined detection, classification, and localization of various complex signals in images. We adopted a classification compensation strategy combining mean and majority filtering by accurately locating the coordinates of dead pixels and optimizing the compensation effect, lossless compensation of α-particle response signals under radiation damage interference is achieved. The proposed algorithm was verified experimentally. The results of this study provide support for improving the mechanism of α-particle radiation effects on CMOS APS as well as drive the development and enhancement of α-particle detection technology.

2 Materials and methods

2.1 Samples and radioactive resource

The Onsemi MT9P031 CMOS active pixel sensor was used as an experimental sample. Its pixel size is 2.2 μm × 2.2 μm, the number of effective pixels is 2592 (H)×1944 (V), the power supply voltage is 1.7 V−3.1 V, the power consumption is 381mW, and the analog-to-digital converter integrated on the sensor provides 8-bit data output. During the experiment, the white balance control system, automatic black balance calibration, noise reduction, and exposure compensation were turned off and the integration time and gain were set manually.

A ^{241}Am radioactive source was used in the experiment. The characteristic energy of the radioactive source was 5.48 MeV, and the fluence rate was 8.56×10^3 cm$^{-2} \cdot$ s^{-1}, as measured using an ORTEC four-channel α spectrometer. The ambient temperature was approximately 27 °C, the nonuniformity of the radiation source was less than 5%, and the radioactivity was 33 kBq. The distance between the sensor and radioactive source was fixed, and the α-particle fluence rate was the same during the experiment. An 3 μm aluminum film was used to isolate the interference of visible light on the sensor. Physical radioactive sources and their energy spectra are shown in Fig. 1a and Fig. 1b.

2.2 Experimental setup

The experimental system included a CMOS active pixel sensor module, and data acquisition and analysis software that used a USB high-speed interface for communication and data transmission. The sensor module included an iCamera mainboard and a CMOS APS sensor board. The mainboard module is an iCamera 51 microcontroller used for the acquisition, preprocessing, and transmission of APS signals with a sampling frequency of 25 Hz. Data acquisition and analysis software was used to read, analyze and store the response data. The experimental setup is illustrated in Fig. 1c, Fig. 1d and Fig. 1e.

The experimental plan and parameter settings are listed in Table 1. Sensor pedestal data were measured and stored prior to the irradiation experiment. During the irradiation

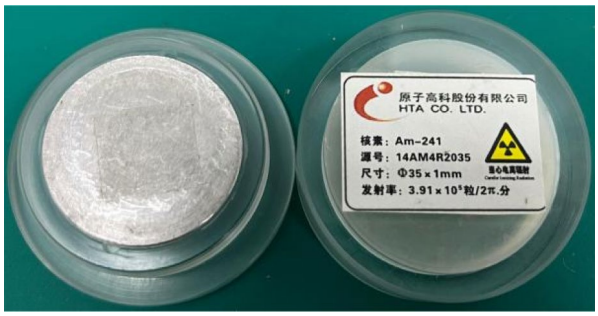

(a)

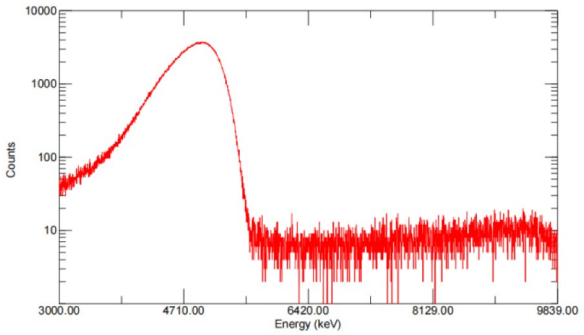

(b)

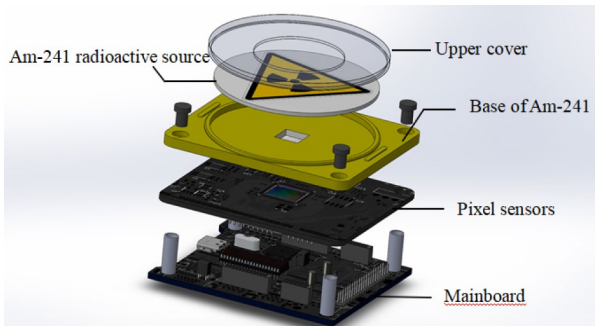

(c)

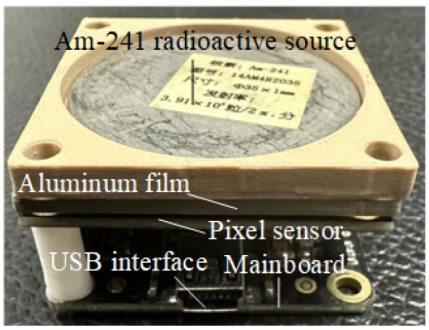

(d)

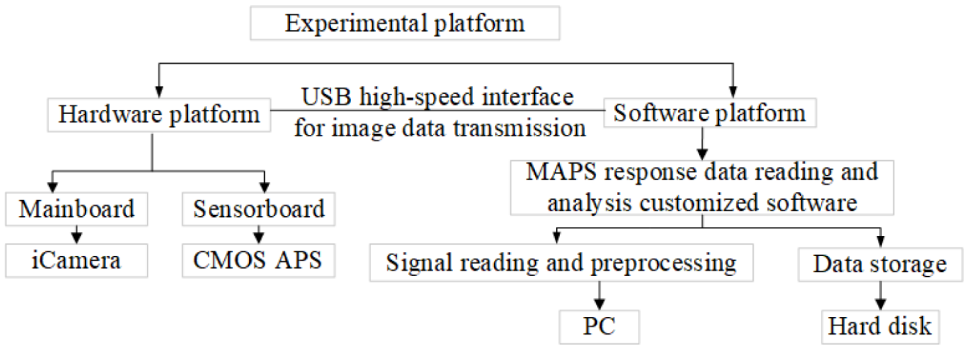

(e)

Fig. 1 (Color online) Experimental samples and experimental system diagram. **a** Image of ^{241}Am radioactive source; **b** (Color online) Energy spectrum in ^{241}Am; **c** Experimental module schematic diagram; **d** Experimental module physical diagram; **e** Experiment system

Table 1 Experimental plan and parameter settings

Step	Experimental type	Time (h)	Gain (dB)	Integral time (ms)
1	Before irradiation	0 (1 times sampling)	5–15	0–90
			50/100	0–90
2	Under irradiation	0 to 87 (29 times sampling)	5–15	0–90
3	After irradiation	0 to 87 (29 times sampling)	50/100	0–90

experiment, the radiation source was removed every 3 h to collect dark image data. The data storage format was "BMP" file format, and the frame sampling rate was 1 s to store one frame of image.

3 Radiation response

Owing to the influence of the gain settings on the amplification factor of each pixel's response signal to α particles, the characteristics and distribution of the α response events are affected. As shown in Fig. 2a shows the distribution map and Gaussian fitting curves of the response signals with an integration time of 22.5 ms for different gain settings. The experimental results indicated that when the gain was set to 8 dB or lower, the characterization measurement of the α-radiation response signal was in an

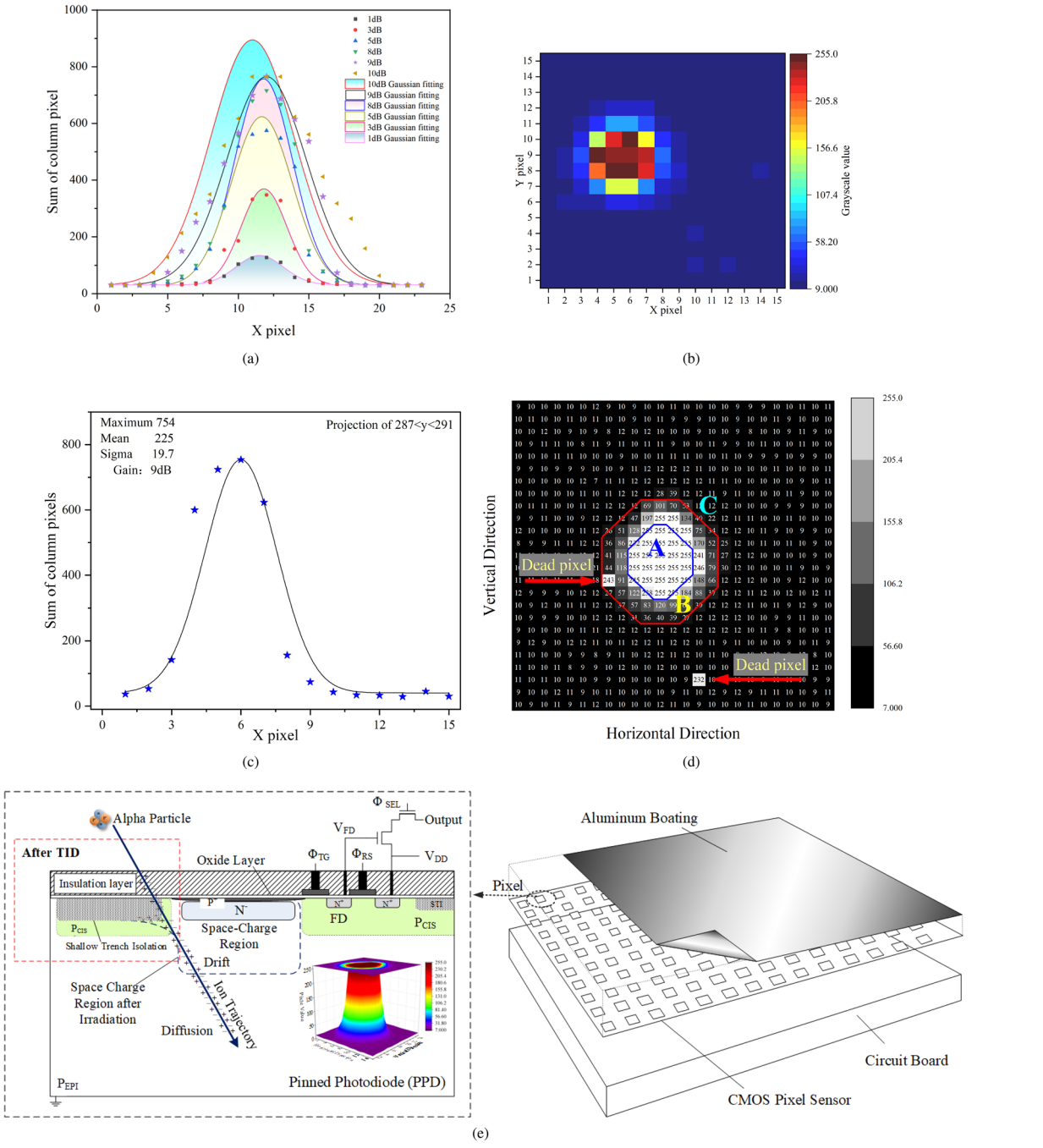

Fig. 2 (Color online) Heatmap and Gaussian fitting of the response signal distribution at different gains, and schematic diagram of the α radiation response. **a** Pixel distribution of response signals and Gaussian fitting under different gains; **b** 9 dB response signal heatmap; **c** 9 dB response signal pixel distribution and Gaussian fitting; **d** 50 dB response signal heatmap; **e** Schematic diagram of α particle radiation effects on a CMOS APS

unsaturated state, as indicated by a single point at the peak falling below the fitting curve. When the gain is set to 10 dB, the sensor parameter setting is in an oversaturated state, characterized by multiple points at the peak falling below the fitting curve. When the gain is set to 9 dB, the peak of the response signal coincides with the vertex of the Gaussian fitting curve, indicating an optimal gain setting. The cross-sectional heat map and distribution map of the 9 dB response signal are shown in Fig. 2b and Fig. 2c, and Gaussian curve fitting was performed.

Although a higher gain may cause distortion in the response signal, it also makes the response signal more pronounced, aiding in distinguishing the signal from the pedestal signal. As shown in Fig. 2d, a heatmap of the gray value distribution of the α response signal is presented under the conditions of a 50 dB gain and an integration time of 22.5 ms. As illustrated, the α response signal exhibits a distinct "target-ring" distribution pattern. In central region A, the pixel values were nearly saturated, with gray values close to 255. Region B is the "ring band" of the α response signal, characterized by similar gray values for pixels on the same ring, but significant differences in gray values between different rings. In this region, the pixel values exhibit a gradient distribution that decreases sharply from the inside to the outside. This is because α particles have high energies, typically between 3 MeV and 5 MeV, with strong ionization capabilities but weak penetration abilities. Consequently, the energy of α particles incident on the sensor surface is almost entirely deposited within the pixels. The size of the pixel area affected by the response signal is related to the energy of the α particles and the number of response signals in the frame image is related to the fluence of the α particles. Region C is referred to as the "external region", which represents noise or pedestal pixel values under dark conditions. The red arrows in the figure indicate the dead pixels, which are described in detail in the next section on radiation damage.

The principal diagram of the α particle radiation effects on a CMOS APS is shown in Fig. 2e. When α particles enter the interior of a pixel, electron–hole pairs are generated by ionization within and near the space-charge region of the photodiode structure. These electron–hole pairs are collected and produce a current under the influence of the built-in electric field, thereby forming a response signal. This is represented by regularly shaped white spots in the frame image. Therefore, a correlation between the energy deposition of α particles and pixel values is evident.

4 Radiation damage

4.1 Radiation damage pattern

Figure 3a shows the distribution of radiation damage noise within 24 h. As shown, the values of each irradiated pixel are generally less than 20, primarily because of the dark current caused by manufacturing defects in the sensor itself, which is known as the pedestal. With prolonged irradiation time and increased total radiation dose, the number of pixels within the 30–255 gray range increases, indicating an increase in noise. After further irradiation, some pixels undergo irreversible damage, losing their ability to collect charge. These pixels are known as dead pixels. Unlike radiation response signals, dead pixels are typically distributed randomly across the entire APS. A key characteristic is their fixed presence across consecutive frames, with positions and intensities unaffected by parameters and irradiation conditions. Therefore, if the pixel values at the same pixel position in three consecutive frames were identical and significantly higher than neighboring pixels, they were identified as dead pixels.

The types and characteristics of damage patterns in the CMOS APS are shown in Fig. 3b. While setting a threshold to subtract the pedestal can mitigate the pedestal's impact on the response signal statistics, it cannot eliminate the interference of radiation damage on the response signals. In addition, dead pixels significantly disrupted the measurement results of α particles.

4.2 Quantitative analysis of α radiation damage

Based on the assessment of α radiation damage patterns and their characteristics in the CMOS APS, precise identification and localization of dead pixels and noise in the output frame images after sensor damage can be achieved. This allowed us to obtain the quantity and positional information of the dead pixels and noise in the frame images at different irradiation times. Figure 3c shows the identification and localization of the dead pixels in a partial area of the frame image. In the figure, "P" represents dead pixels, and the red boxes indicate response signals. This method enables the accurate detection of failed sensor pixels, which is crucial for suppressing and compensating radiation noise.

Figure 3d depicts the relationship curve showing the variation in noise and dead-pixel counts over the irradiation time under continuous irradiation conditions for 72 h. As shown, with prolonged irradiation time and increased total radiation dose, the pedestal pixel values and number of dead pixels in the CMOS APS continuously increase.

It can be observed that the amount of noise increases initially and then levels off with increasing irradiation time, whereas the number of dead pixels continues to rise steadily with irradiation time. This indicated that as the accumulated dose increased, the pedestal pixel values continued to increase. This is because of the increase in trap charges generated at the Si/SiO_2 interface of the shallow trench isolation (STI) within pixel units with increasing total radiation dose. This phenomenon enlarges the depletion region and

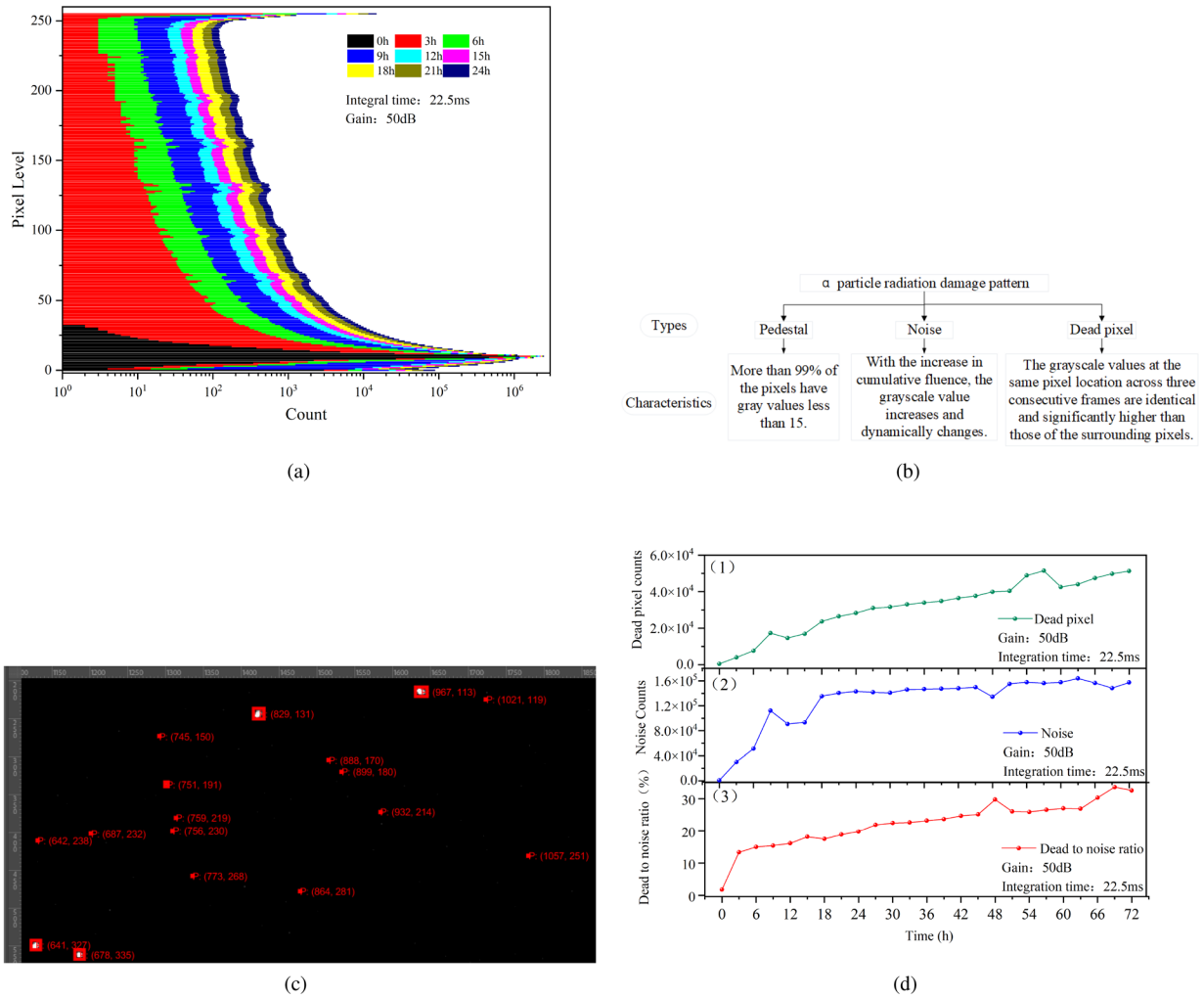

Fig. 3 (Color online) Types, characteristics, and temporal variations of radiation damage. **a** Histogram of irradiation damage changing with irradiation time; **b** damage mode type and characteristic relationship diagram; **c** identification and localization of dead pixels in the frame image; **d** variation of dead pixels, noise, and dead-to-noise ratio with irradiation time

pushes it closer to the STI structure, leading to an increase in dark current. Some pixels may be more susceptible to radiation damage due to their manufacturing processes. With an increase in the total irradiation dose, the pixel values of the vulnerable pixels reach saturation, and some pixels may undergo natural annealing and recovery after damage. However, the number of dead pixels that have lost their charge collection capability continues to increase.

The proportional relationship between the dead-pixel data in Fig. 3d(1), and the noisy data in Fig. 3d(2) to derive the curve in Fig. 3d(3) showing the variation in the dead-to-noise ratio over time. The dead-to-noise ratio increased continuously with increasing irradiation time, indicating that the impact of radiation damage on sensor performance gradually intensified, with an increasing number of pixels becoming dysfunctional. After 72 h of irradiation, the dead-to-noise ratio reaches 32.54 %.

5 Radiation damage compensation

5.1 Characteristics and detection methods of dead pixels

Figure 4a shows the histogram of noise and response signals within a 25 × 25 pixel area after 24 h of irradiation. Figure 4b shows the 3D distribution with dead pixels in the response signal. Significant differences exist between response signals and noise characteristics. The α response signal covers an area of 3 × 3 pixels or larger, with gray values decreasing from the central pixel outward. The central pixel has a gray value around 250, consistent with the target-ring distribution. Dead pixels appear as isolated pixels with higher values than adjacent pixels, ranging from 50 to 255. Before irradiation, CMOS APS pedestal pixel values were below 20. Irradiation increases pedestal pixel values and

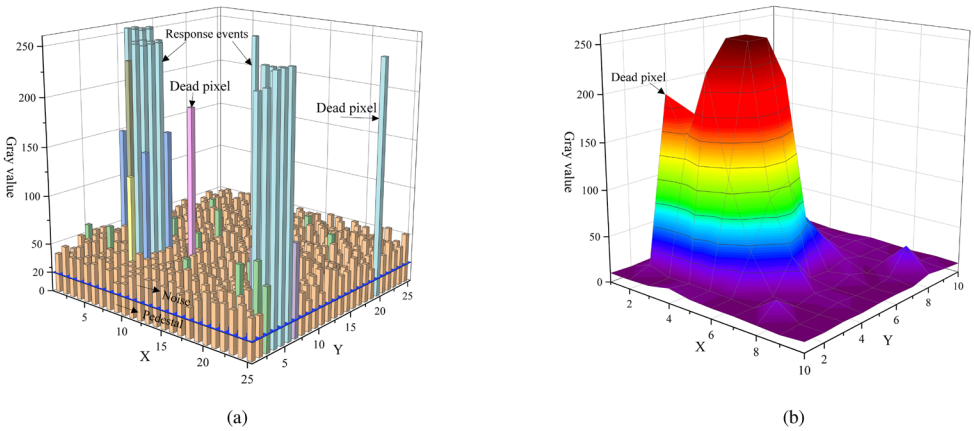

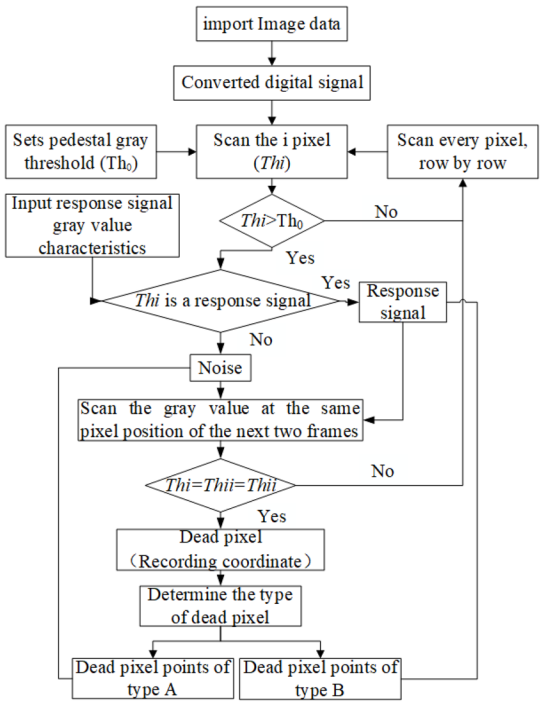

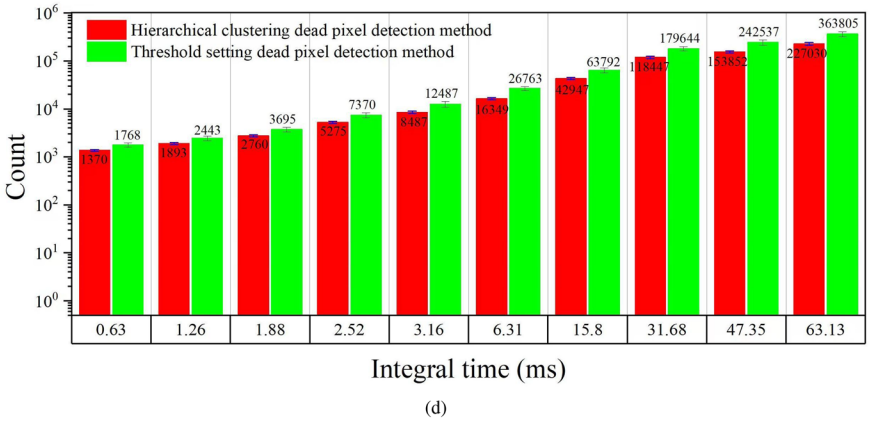

Fig. 4 (Color online) Characteristics and detection of dead pixels. **a** Histogram of noise and response signals; **b** characteristics of dead pixels in the response signal; **c** logic block diagram of dead-pixel detection method; **d** histogram of the number of dead pixels detected by the two methods under different integration times

damages pixels. When establishing statistical relationships between pixel values and α particle radiation, dead pixels affect the signal-to-noise ratio and α response signal statistics, necessitating radiation damage compensation research.

Based on the previous analysis of the response signal and the characteristics of the dead pixels, as shown in Fig. 4a and Fig. 4b, dead pixels are classified into two categories: one type is dead pixels within the response signal and dead pixels within the pedestal or noise. By converting the imported N images into array data and using the analyzed gray values, response signal characteristics, and dead pixels for hierarchical clustering to identify pixel points, a hierarchical clustering dead-pixel detection method was proposed, as shown in Fig. 4c.

In the figure, Th_0 represents the pedestal noise threshold, which is obtained by calculating the average pixel value of the dark image before irradiation. The calculation formula is as follows Eq. (1):

$$\mathrm{Th}_0 = \frac{1}{N \times j \times k} \sum_{n=1}^{N} \sum_{i=1}^{j \times k} E_{n,i \times k}, \tag{1}$$

where N represents the total number of frames and $E_{n,(i \times k)}$ represents the pixel value matrix of the n-th frame, where j and k are the horizontal and vertical pixel matrix coordinates, respectively.

In this study, 300 dark image frames before irradiation were selected for the calculation. The calculation results show that the average pixel grayscale value was 15 or more than 99% of the pixels with a value less than 15. Therefore, in this study, the pedestal noise threshold Th_0 was set to 15.

When determining whether the n-th imported frame image contains dead pixels, the pixel points are scanned row by row and then column by column. If the gray value of a scanned pixel point exceeds the threshold, then it is considered a potential response signal or noise. The target-ring classification characteristics of the response signal were imported to determine whether the point was a response signal. If it does not conform to the target-ring distribution characteristics, then it is considered noise. Then, further analyze the identified response signal or noise and continued scanning the gray values of the pixel points in the same position for the next two frames. If the gray values of this pixel are equal for three consecutive frames, the pixel is judged to be a dead pixel. Based on the location of the dead pixels, they were classified into two types: Type-A dead pixels were located outside the response signal and type-B dead pixels were located within the response signal.

A threshold-setting method and hierarchical clustering dead-pixel detection method were proposed. The dead pixels in the frame images were counted, and a histogram of the dead-pixel count detected using the two methods at different integration times is shown in Fig. 4d. The number of dead pixels detected by the threshold-setting method was generally higher than that detected by the hierarchical clustering dead-pixel detection method. This is because the threshold-setting method counts noise above the set threshold as dead pixels, which includes damaged pixels that have not yet died. The detection error of this method across multiple frames was higher than that of the hierarchical clustering detection method. The detection method proposed in this study is more accurate and has fewer errors.

5.2 α radiation damage compensation method

A dead-pixel compensation method was proposed based on the characteristics of the dead pixels, as shown in Fig. 5. For type-A dead pixels (i.e., dead pixels in noise), compensation was achieved using a majority filtering method. The compensation algorithm is expressed by Eq. (2):

$$I_c = I_{\mathrm{PM}}, \tag{2}$$

where I_c is the gray value after dead-pixel compensation and I_{PM} is the gray value of the noise or pedestal pixel with the largest number in the current frame image.

For type B dead pixels, i.e., dead pixels in the response signal, based on the characteristics of the target-ring distribution, we propose to mainly use the idea of mean filtering using the interpolation of adjacent pixels to replace the output of the dead pixel. When the dead pixel is in the "center point" region, since the gray value of the pixel in the center point region is relatively high in the entire response signal characteristics, the dead pixel has little effect on it.

The compensation method is to calculate the average pixel gray value of the entire center point region as the compensation pixel gray value of the dead pixel after deducting the damaged pixel point; when the dead pixel is in the "ring band" region, the average value of the current ring is used as the compensation pixel gray value of the dead pixel; when the dead pixel is in the "external region", the noise gray value of this region is not much different from that of the sensor as a whole, and the detected dead pixel can be replaced and compensated by the above-mentioned type-A

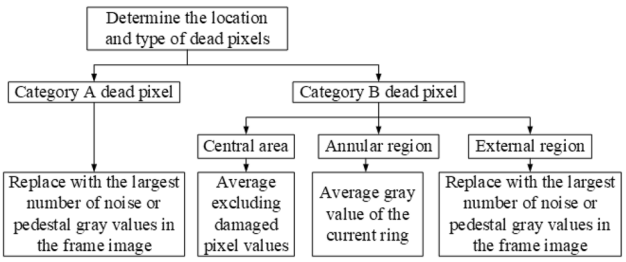

Fig. 5 Logic block diagram of dead-pixel compensation method

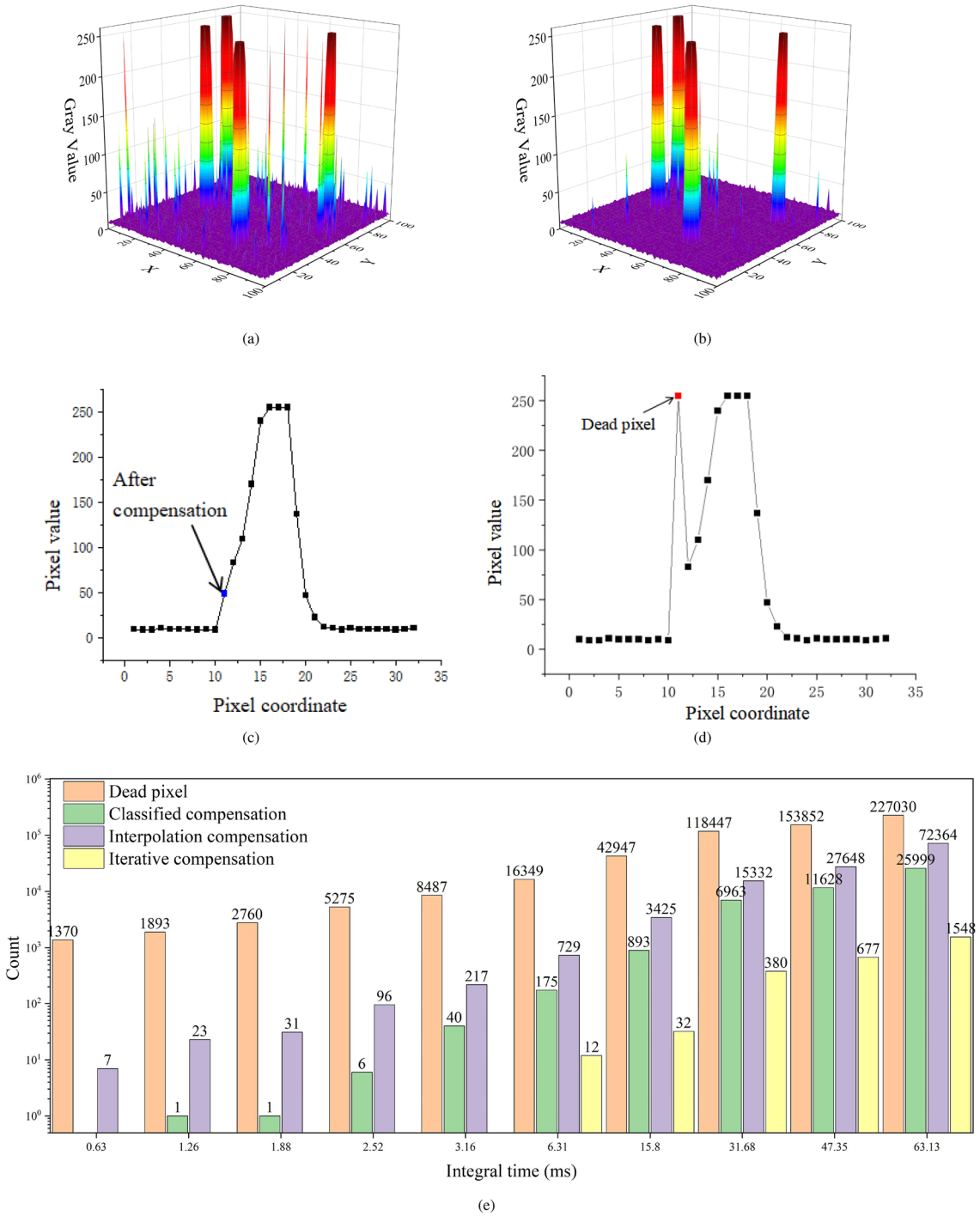

Fig. 6 (Color online) Radiation damage effect of α particles. **a** Dead pixel before compensation; **b** dead pixel after compensation; **c** horizontal cross-sectional gray values before compensation; **d** horizontal cross-sectional gray values after compensation; **e** relationship between the count of dead pixels before and after compensation with integral time

dead-pixel compensation method. The mean filter processing algorithm is as follows Eq. (3):

$$V_I = \frac{\sum_{i=1}^{N-I}(V_{iD})}{N-I}, \tag{3}$$

where N is the number of pixels in different "target-ring" region in the response signal, V_I is the gray value after dead-pixel compensation, I is the number of dead pixels in the "target-ring" region, and V_{iD} is the gray value of the pixel in the "target-ring" region where the dead pixel is located.

5.3 α radiation damage compensation effect

In this study, Python was used to write the algorithms for image data processing on a PC. The time required for this algorithm to perform dead-pixel detection or compensation processing on a frame of image is 0.04 s (±0.005 s), and the required storage space is 66 kB. To reduce statistical errors, approximately 300 image frames were processed for each parameter condition. Therefore, the image data processing speed under a single-parameter variable was approximately 12 s, and the occupied memory was approximately 19.3 MB. Figure 6a and Fig. 6b show a comparison bar chart of the compensation effects before and after. After applying the compensation algorithm, the number of dead pixels decreased significantly, whereas the response signal remained unaffected. The compensation algorithm does not interfere with the response signal data. Therefore, this compensation algorithm effectively achieved dead-pixel compensation without affecting the response signal.

Figure 6c and Fig. 6d depicts the distribution of the pixel gray values of the cross section of the response signal before and after compensation. The red pixels in the image before compensation represent dead pixels, which clearly indicate the location and degree of radiation damage. It can be observed from the compensated image that the proposed compensation algorithm based on the target-ring distribution characteristics compensates for the red dead pixels in the original Fig. 6c, the pixel value is replaced with that of the blue pixel in Fig. 6d. The experimental results show that the radiation noise compensation method proposed in this study can effectively compensate for dead pixels and reduce the interference of radiation damage on the image information data, thereby improving the accuracy of the APS's response to α-particles.

The integral time is closely related to the characterization of the dead pixels caused by radiation damage. Longer integration times can improve the sampling efficiency of alpha particle response signals, but they can also increase the pedestal owing to the dark currents generated by radiation damage during the integration period. Figure 6e shows the relationship between the number of dead pixels before and after compensation using the two methods under different integral conditions. As shown in the figure, the compensation effect of the distribution compensation strategy adopted in this study is better than that of the current single interpolation compensation method. Through multiple iterations of the compensation algorithm, the number of dead pixels can be further effectively reduced when the integral time exceeds 6.31 ms.

6 Conclusion

In this study, experiments were conducted on the alpha particle radiation response and damage of CMOS APS by studying the characteristics of the response events and damage modes. It quantitatively characterizes radiation damage and proposes a method for detecting, locating, and compensating for radiation damage noise. The conclusions drawn from the experiments are as follows:

1) For the selected samples in this study, the characterization accuracy of the response signal generated by alpha particles was the highest when the gain was set to 9 dB. Alpha particle response events exhibit distinct "target-ring" distribution characteristics.
2) As the cumulative dose increased, the pedestal of the CMOS APS increased and eventually became saturated. However, the number of dead pixels continues to increase. Although some pixel damage may be recovered through natural annealing, the dead-to-noise ratio continues to increase with prolonged irradiation time.
3) The dead pixels are divided into two categories according to their location: those located inside and outside the response signal. Using the target distribution characteristics of the alpha response signal, the mean filter method is used to compensate for dead pixels located inside the response signal and the majority filter method is used to compensate for dead pixels located outside the response signal. Multiple iterations of the compensation algorithm can effectively reduce the number of dead pixels caused by an increase in integration time.

Author contributions All authors contributed to the study conception and design. Material preparation, data collection, and analysis were performed by Cui-Yue Wei, Zhi-Wei Qin, and Shu-Liang Zou. The first draft of the manuscript was written by Shou-Long Xu, and all authors commented on previous versions of the manuscript. All authors read and approved the final manuscript.

Data availabilty The data that support the findings of this study are openly available in Science Data Bank at https://cstr.cn/31253.11.sciencedb.j00186.00909 and https://www.doi.org/10.57760/sciencedb.j00186.00909.

Declarations

Conflict of interest The authors declare that they have no conflict of interest.

References

1. J.H. Lee, J.I. Byun, D.M. Lee, In-situ $CeBr_3$ gamma-ray spectrometry for radioactivity analysis of soil. J. Radioanal. Nucl. Chem. **321**, 599–603 (2019). https://doi.org/10.1007/s10967-019-06621-7
2. Z.Q. Wu, J.X. Cheng, M. Xu et al., Standoff alpha radiation measurement of surface contamination based on radioluminescence. App. Radiat. Isotopes **199**, 110867 (2023). https://doi.org/10.1016/j.apradiso.2023.110867
3. N. Dufour, J. Dumazert, E. Barat et al., Measurement of low-activity uranium contamination by gamma-ray spectrometry for nuclear decommissioning. Nucl. Instrum. Methods **951**, 162976 (2021). https://doi.org/10.1016/j.nima.2019.162976
4. S.B. Liu, F. Lin, Z.K. Fan et al., Comparison of radon exhalation rate measurements on reference device in open and closed loop by AlphaGUARD in flow-through mode. Radiat. Prot. Dosim. **199**, 1151–1157 (2023). https://doi.org/10.1093/rpd/ncad063
5. N.K. Sethy, S. Singh, V.N. Jha et al., Field evaluation of an encapsulated ^{226}Ra – ^{222}Rn source. Mapan **39**, 131–137 (2024). https://doi.org/10.1007/s12647-023-00720-3
6. M.C. Niu, H.W. Liang, R.R. Fan et al., Research on the application of pulse shape discrimination method in (n, lcp) reaction cross-section measurements. Nucl. Instrum. Methods A **1051**, 168–215 (2023). https://doi.org/10.1016/j.nima.2023.168215
7. Y.M. Gledenov, V.V. Nesvizhevsky, P.V. Sedyshev et al., A method to measure neutron polarization using P-even asymmetry of γ-quantum emission in the neutron-nuclear interaction. Phys. Atom. Nuclei **75**, 781–784 (2012). https://doi.org/10.1134/S1063778812030076
8. Y.N. Zhang, Q. Liu, H.B. Liu et al., Study of a sealed high gas pressure THGEM detector and response of alpha particle spectra. Chin. Phys. C **41**, 046001 (2017). https://doi.org/10.1088/1674-1137/41/4/046001
9. N. Hasebe, M. Miyajima, E. Shibamura et al., α-particle spectrometer based on xenon gas ionization chamber using coplanar electrodes. Nucl. Instrum. Meth. A **925**, 123–127 (2019). https://doi.org/10.1016/j.nima.2019.01.079
10. Q. Du, S.T. Lin, H.T. He et al., Response of gadolinium doped liquid scintillator to charged particles: measurement based on intrinsic U / Th contamination. J. Instrum. **13**, P04001 (2018). https://doi.org/10.1088/1748-0221/13/04/P04001
11. K. Yasuda, S. Usuda, H. Gunji, Properties of a YAP powder scintillator as alpha-ray detector. Apple Radiat. Isotopes **52**, 365–368 (2000). https://doi.org/10.1016/S0969-8043(99)00179-7
12. N. Stevanovic, V.M. Markovic, M. Milosevicx et al., Correlations between track parameters in a solid-state nuclear track detector and its diffraction pattern. Radiat. Phys. Chem. **193**, 109986 (2022). https://doi.org/10.1016/j.radphyschem.2022.1099862
13. T.L. Cardoso, S.T. Oliveira, R.M. Marques Pinheiro et al., Radon dosimetry using solid state nuclear track detectors in different environments: a review. Apple Radiat. Isotopes **186**, 110217 (2022). https://doi.org/10.1016/j.apradiso.2022.110217
14. A. Gola, K. Majumdar, G. Casse et al., First demonstration of the use of LG-SiPMs for optical readout of a TPC. J. Instrum. **15**, P12017 (2020). https://doi.org/10.1088/1748-0221/15/12/P12017
15. Y. Li, H. Yi, Y.K. Sun et al., Performance study of the multi-purpose time projection chamber (MTPC) using a four-component alpha source. Nucl. Instrum. Methods **1060**, 169045 (2024). https://doi.org/10.1016/j.nima.2023.169045
16. M. Cortesi, J. Pereira, D. Bazin et al., Development of a novel MPGD-based drift chamber for the NSCL/FRIB S800 spectrometer. J. Instrum. **15**, 3–25 (2020). https://doi.org/10.1088/1748-0221/15/03/P03025
17. Z.W. Qin, S.L. Xu, H.F. Dong et al., Research on calculation method of radiation response eigenvalue of a single-chip active pixel sensor. Sensors **22**, 4815 (2023). https://doi.org/10.3390/s22134815
18. M. Tsutsumi, T. Meguro, A. Takeyama et al., Ntegrated 4H-SiC photosensors with active pixel sensor-type circuits for MGy-class radiation hardened CMOS UV image sensor. IEEE Electr. Dev. Lett. **69**, 6329–6341 (2022). https://doi.org/10.1109/TSP.2021.3127679
19. S.L. Xu, S.L. Zou, Y.C. Han et al., Study on the availability of 4T-APS as a video monitor and radiation detector in nuclear accidents. Sustainability **10**, 2172 (2018). https://doi.org/10.3390/su10072172
20. R. Guo, Y. Li, T. Blu et al., Vector-FRI recovery of multi-sensor measurements. IEEE Trans. Signal Process. **70**, 4369–4380 (2022). https://doi.org/10.1109/TSP.2022.3204402
21. Z. Tang, Y. Fang, Z. Huang, An untrimmed BJT-based temperature sensor with dynamic current-gain compensation in 55-nm CMOS process. IEEE Trans. Circuits-II **66**, 1613–1617 (2019). https://doi.org/10.1109/TCSII.2019.2921889
22. L.M. Carvalho Freitas, F. Morgado-Dias, Thermal readout noise comparison of classical constant bias APS and switching bias APS used in CMOS image sensors. Analog Integr. Circ. Sig. Process **111**, 267–275 (2022). https://doi.org/10.1007/s10470-021-01964-2
23. S.L. Xu, S.L. Zou, Y.C. Han et al., Obtaining high-dose-rate γ -ray detection with commercial off-the-shelf CMOS pixel sensor module. IEEE Sens. J. **19**, 6729–6735 (2019). https://doi.org/10.1109/JSEN.2019.2912198
24. H. Deng, H. Zhang, H. Zhao et al., γ radiation image denoising method based on speckle splitting. Sign. Imag. Vedio Proc. **17**, 1391–1399 (2023). https://doi.org/10.1007/s11760-022-02347-4
25. J. Feng, J. Fu, Y.D. Li et al., Mechanism of ionization damage in large eight-transistor complementary metal-oxide-semiconductor color image sensors. J. Nanoelectron. Optoelectron. **16**, 1755–1761 (2021). https://doi.org/10.1166/jno.2021.3136
26. S. Haro, M. Bessia, F. Perez et al., Soft X-rays spectroscopy with a commercial CMOS image sensor at room temperature. Radiat. Phys. Chem. **167**, 108354 (2020). https://doi.org/10.1016/j.radphyschem.2019.108354
27. R.P. Alikunju, S. Kearney, R. Moss et al., Effect of different scintillator choices on the X-ray imaging performance of CMOS sensors. Nucl. Instrum. Methods A **1050**, 168136 (2023). https://doi.org/10.1016/j.nima.2023.168136

28. S. Staeck, Y. Kayser, J. Baumann et al., Towards soft x-ray fluorescence measurements in the laboratory using a laser-produced plasma source and a complementary metal-oxide semiconductor detector. J. Instrum. **16**, P03033 (2021). https://doi.org/10.1088/1748-0221/16/03/P03033
29. J. Teng, L.Q. Shan, B. Zhu et al., A compact online proton spectrometer for diagnosis of picosecond intense-laser accelerated protons. AIP Adv. **13**, 115008 (2023). https://doi.org/10.1063/5.0171418
30. X. Zha, M.M. El-Gomati, L. Chen et al., Direct detection of low-energy electrons with a novel CMOS APS sensor. IEEE Trans. Electron. Dev. **59**, 3594–3600 (2012). https://doi.org/10.1109/TED.2012.2219623
31. Y.C. Han, S.L. Xu, Y.J. Huang, Real-time monitoring method for radioactive substances using monolithic active pixel sensors (MAPS). Sensors **22**, 3919 (2022). https://doi.org/10.3390/s22103919
32. S.L. Xu, Z.W. Qin, Y.C. Han et al., Ultrawide-range radiation detection based on dynamic identification and analysis of the response of a monolithic active pixel sensor. Opt. Express **30**, 14134–14145 (2022). https://doi.org/10.1364/OE.458752
33. Z.J. Wang, Y.Y. Xue, X.Q. Guo et al., Measurement and analysis of the conversion gain degradation of the CIS detectors in harsh radiation environments. Nucl. Instrum. Methods **895**, 35–39 (2015). https://doi.org/10.1016/j.nima.2018.04.002
34. Y. Jiang, L. Wen, J. Feng et al., Research on proton displacement damage effects in charge-domain accumulation type TDI CMOS image sensors. Radiat. Eff. Defect. Solids **179**, 811–812 (2024). https://doi.org/10.1080/10420150.2024.2311826
35. M. Deveaux, Progress on the radiation tolerance of CMOS monolithic active pixel sensors. J. Instrum. **14**, R11001 (2019). https://doi.org/10.1088/1748-0221/14/11/R11001
36. F.A. Bessia, M. Pérez, M.S. Haro et al., Charged particle radiation damage in CMOS image sensors after thermal neutron irradiation. IEEE Trans. Nucl. Sci. **65**, 2793–2801 (2018). https://doi.org/10.1109/TNS.2018.2874191
37. V. Premachandran, K. Ramakrishna, Measuring the effectiveness of bad pixel detection algorithms using the ROC curve. IEEE Trans. Consum. Electr. **56**, 2511–2519 (2010). https://doi.org/10.1109/TGRS.2019.2948890
38. J. Zhang, S. Masanori, O. Takayuki, That's BAD: blind anomaly detection by implicit local feature clustering. Mach. Vision Appl. **35**, 31 (2024). https://doi.org/10.1007/s00138-024-01511-9
39. A. Sadri, H.J. Marjan, Automatic bad-pixel mask maker for X-ray pixel detectors with application to serial crystallography. J. Appl. Crystallogr. **55**, 1549–1561 (2022). https://doi.org/10.1107/S1600576722009815
40. Z. Qiao, X. Shu, Coupled neurons with multi-objective optimization benefit incipient fault identification of machinery. Chao. Soliton. Fractal. **145**, 110813 (2021). https://doi.org/10.1016/j.chaos.2021.110813
41. D.G. Zhang, B. Cheng, L. Shi et al., A destriping algorithm for SDGSAT-1 nighttime light images based on anomaly detection and spectral similarity restoration. Remote Sens.-Basel **14**, 5544 (2022). https://doi.org/10.3390/rs14215544
42. P. Skibiński, R. Czesław, Bad pixel correction method for locally analytic images: application to infrared spectroscopy. J. Electron. Imaging **225**, 043020 (2013). https://doi.org/10.1117/1.JEI.22.4.043020